Digest Journal of Nanomaterials and Biostructures Vol. 19, No. 4, October-December 2024, p. 1765-1789

Sustainable visible light-driven catalysis using Ca-doped ZnO nanoparticles via sol-gel methodology

Z. A. Sandhu [a], F. Ali [b], A. Nazir [b], A. Mehmood [a], M. A. Raza [a,*], K. Bibi [b], A. Iqbal [b], M. K. Hussain [c], M. Zain [d], B. Saleh [e], H. T. Ali [e]

[a]*Department of Chemistry, Faculty of Science, University of Gujrat, Hafiz Hayat Campus, Gujrat, 50700, Pakistan*

[b]*Department of Physics, Faculty of Science, University of Sialkot, Sialkot, 51310, Pakistan*

[c]*Research School of Chemistry, Australian National University, Canberra ACT 2601, Australia*

[d]*Department of Chemistry and Chemical Engineering, Lahore University of Management Sciences*

[e]*Department of Mechanical Engineering, College of Engineering, Taif University, Kingdom of Saudi Arabia*

In current research, we investigated the optical parameters of ZnO based nanomaterials (pure and Ca-doped ZnO nanostructures). X-ray diffraction study examined that nanostructures had good crystallinity and phase purity. Furthermore, energy-dispersive X-ray spectroscopy reported the composition of nanomaterials and scanning electron microscopy (SEM) also illustrated the surface morphology of nanomaterials. Photoluminescence and UV-visible spectroscopy were employed to explore the optical features. It was observed from results that 3% calcium-doped zinc oxide exhibited highest efficiency in the degradation of both MB and MO dyes. Notably, the highest degradation efficiency achieved for MB and MO was 84% and 89%, respectively.

(Received September 10, 2024; November 18, 2024)

Keywords: ZnO-NPs, Sol-gel, Photocatalysis, Waste water treatment, Methylene blue

1. Introduction

The presence of polluted water can result in detrimental consequences for humans, encompassing contamination within the food chain, disruption of ecosystems, diminished biodiversity, economic repercussions, and environmental degradation [1]. Water contamination is a prevalent global issue stemming from various geological and anthropogenic sources [2]. Various treatment strategies [3] such as primary (physiochemical and chemical), secondary (chemical and biological), tertiary (physical and chemical) and sludge treatment (tipping, incineration and recycling) [4] have being used. These techniques use the phenomenon of biosorption, bioremediation [5], coagulation, flocculation, precipitation, ion-exchange, membrane filtration, reverse osmosis, nanofiltration, and electrochemical [6]. The methodology encompasses chemical, physical, and biological approaches capable of achieving partial removal [3] leading towards advanced oxidation process. They have practical and effective capacity over wide range of ozonation and UV irradiation [7]. Numerous studies have been performed by various researchers in the field of wastewater treatment, exploring techniques such as plasma, ultrasound, electron beams and electrochemical methods. Effective methods for treating industrial wastewater have been the topic of much more study in current decade [8].

Wastewater treatment generally falls into two categories: organic and inorganic. Inorganic treatments are particularly recommended for treatment of wastewater owing to their essential leads over organic counterparts. Dyes are predominantly dispersible pollutants, playing a important part in the toxicity of the aquatic system [5]. It can be efficiently degraded via photocatalysis by

* Corresponding authors: asamgcu@yahoo.com
https://doi.org/10.15251/DJNB.2024.194.1765

semiconductor nanoparticles [9]. Furthermore, numerous photocatalyst such as ZnO, TiO_2, Bi_2O_3, CdS have been processed [9] but zinc oxide being n-type semiconductor possess greater energy gap 3.37 eV resultant have greater free excitation binding energy [10] is greatly accepted in various research fields [11]. It has capacity due to its large thermal and chemical stability, broader catalytic activity, nontoxicity, lower cost, adjustable band gap and ecologically harmless [9]. Due to intrinsic defect like vacancies, greater photo corrosion [12] there are minor concerns regarding the photocatalytic efficiency of zinc oxide, particularly its limited absorption of UV-Vis or solar light, which restricts its widespread utilization [9]. It has been stated that the visual and electronic parameters [12] would be changed along the enhancement of gas adsorption property [13] and sensor application in different fields [10].

Dyes play a vital part in a wide range of fields, including textiles and cosmetics, because of their ability to contribute color [14]. MB and MO are distinguished by their unique properties and extensive range of uses. These organic dyes have been intensively studied for their possible use in photocatalysis, environmental remediation, and as model contaminants in scientific investigations [15]. They can act as an excellent agent for examining complex chemical and physical phenomena due to their unique features [16]. There are some metals that have great application in the enhancement of zinc oxide like the rare earth elements, transition metals (Mo, Fe, Ti, Co, and Ni) alkali, alkaline earth metals [17]. In this study, Ca doping has an exceptional capacity to modify the visual characteristics and photocatalytic activity of ZnO [18, 19]. Ca inclusion can increase optical absorption in range of visible light while also controlling excitation recombination. Furthermore, due to the changeover of the Zn^{2+} binding sites for the Ca^{2+}, further provision may be formed, such as oxygen deficits, interstitials, amongst others, which might be favourable for photocatalytic process [12]. Moreover, calcium doping can refine the grain dimensions of the nanoparticles, lead to a significant increase in their surface area. This enhanced surface area is particularly beneficial for applications in photocatalysis and adsorption [20, 21]. The radius of calcium cation (Ca^{2+}) is greater than that of zinc cation (Zn^{2+}), which equals to 0.74 Å [22-24]. The size variation leads to the possibility that calcium addition might trigger imperfections inside the structure [25, 26]. Furthermore, the compatibility of the Ca-doped ZnO system is improved and the chance of inducing other undesirable chemical reactions or instability to the material due to chemical instability of calcium, an alkaline earth metal, with zinc is also reduced [13]. Slama et al. (2016) employed sol-gel techniques to prepare $Zn_{1-x}Ca_xO$ nanoparticles, where x is between 0 and 0.05. The absence of the typical secondary phases and the wurtzite single crystalline phase observed in the nanoparticles implied Ca substitution of Zn in the structure. With regards to Ca loading measurements, $Zn_{0.96}Ca_{0.04}O$ exhibited the highest photocatalytic potential [9]. ZnO was already believed to have better photocatalytic activity by the previous study, if calcium dopants were to be employed. The charge carrier quantity increase, grain size decrease, and crystal structure modifications are the main factors in the growth of photocatalytic activity [27].

The main goal of current study is to demonstrate the viability of using visible light-driven catalysis with Ca-doped ZnO nanoparticles as a sustainable approach of purifying industrial wastewater. In addition, we study how well Ca-doped ZnO NPs degrade organic pollutants found in industrial effluent when they are exposed to light. Our synthesized material is more suitable photocatalyst for the degradation of dyes and environment remediation. It showed remarkable photocatalytic as well as cyclic stability performance.

2. Experimental work

2.1. Chemicals and materials

The precursor chemicals that were employed in the fabrication process of doped and pure zinc oxide were obtained from Merck at a purity rate exceeding 99%. The photocatalysis process included the use of methylene orange (MO) and methylene blue (MB), calcium nitrate and zinc nitrate to represent Ca and Zn ions, respectively, ammonia solution to adjust pH, and citric acid. And the process of purification was not required after that, and all chemicals were of analytical standard.

2.2. Synthesis of pure and Ca-doped ZnO nanostructure

Sol-gel technique was utilized to synthesize both pure and Ca-doped ZnO at altered dopant concentrations (1% - 4%, as shown in figure 1). This approach represented an amendment of the sol-gel synthesis procedure [28]. For the preparation of pure zinc oxide, dissolve 2 grams of zinc nitrate ($ZnNO_3$) in 50 milliliters of water, stir, and let it remain for 30 minutes. Then, effectively mix 1 gram of citric acid and stir constantly for 15 minutes. Citric acid was added to the zinc solution gradually while stirring continuously, and the combination was allowed to integrate for approximately fifteen minutes. To maintain the pH at 9, ammonia solution was slowly poured to mixture. The resultant liquid was stirred for six hours, and then heated to 140°C until a thick gel formed. After drying, the gel undergone three water washes to achieve a pH of zero. In order to yield pure ZnO, the powder was grinded and then calcined at 500°C for two hours. Starting materials included zinc nitrate ($ZnNO_3$) 2 g and a calcium dopant (20-80 mg) for the synthesis of calcium-doped ZnO (1%, 2%, 3%, and 4% wt.). After achieving a transparent solution of 2 grams of zinc precursor in 50 ml of water, precisely 30 ml of calcium salt were added as required. This addition was performed before to the incorporation of the citric acid, and the remaining stages followed the alike procedure as detailed previously.

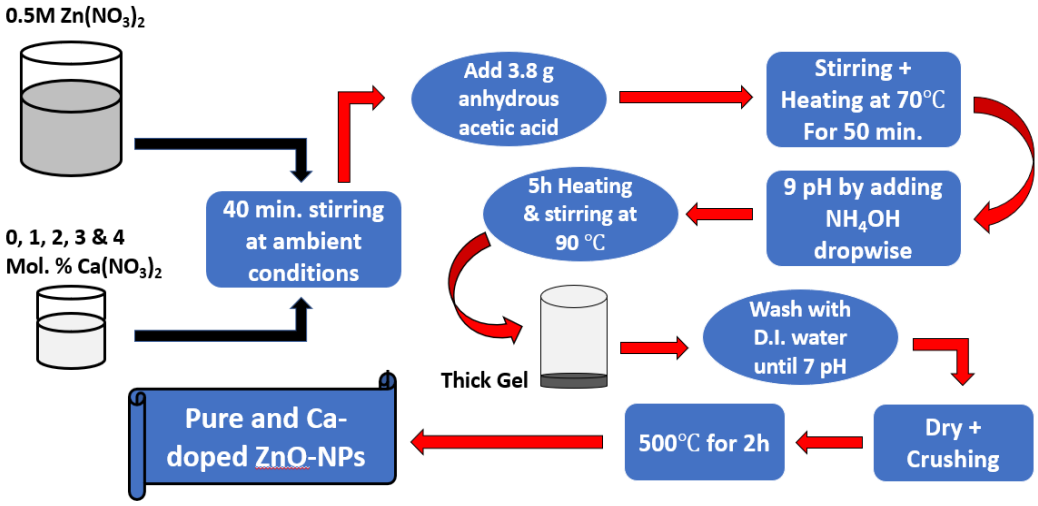

Fig. 1. Flow chart of pure and doped zinc oxide nanostructure preparation.

2.3. Characterization

The synthesized nanostructure was first analyzed using XRD, with a scanning range of 10 to 80 degrees (2θ). The Bruker AXS D8 diffractometer was used, generated Cu (kα) radiation with a wavelength of 1.5406 Å. This was followed by investigation using FESEM (Philips XL30 electron microscope) under an operating voltage of 20 kv, along with EDX analysis to explore the morphology and composition associated with the nanostructure. A UVD-3500 double-beam UV-visible Perkin Elmer equipment was also used to evaluate the synthesized nanostructure's photocatalytic degradation efficiency. The UV-visible spectrum corresponding to the accomplished synthesized nanostructured using range of the wavelength (200-600 nm). The nanostructure photocatalytic and electron-hole recombination processes were tested by the PL technique.

2.4. Photocatalytic application

The purpose of this research was to observe photocatalytic action of pure and Ca-doped zinc oxide nanostructures. A reaction was accomplished in a 10 ppm solution of dye that consisted of 10 mg of the dye and 25 mg of pure or doped zinc oxide for each 200 mm solution of the dye by following the normal procedure. The sample's value of % D (degree of degradation) was calculated

at the end of 120 minutes of radiation exposure. About 2 ml of the reaction mixture was collected and then subjected to 20 minutes of centrifugation at around 3500 rpm to recover the suspended particles. Moreover, model concentration was determined with a UV-Vis spectrophotometer analysis [30]. Equation 1 [31, 32] was used for calculation of percentage degradation.

$$(\%D) = \frac{A_0 - A_t}{A_0} \times 100 \quad (1)$$

At is the value of the dye and its absorption amount that are measured at a specific time after the reaction began, while At=0 is the value of the light at t=0. For kinetic description of the oxidation pseudo-first order kinetics using equation 2 was utilized [33].

$$\ln(A_t) = \ln(A_0) - kt \quad (2)$$

The 'k' value indicates the pseudo first order rate constant (min^{-1}) for radiation, while 't' stands for the time period of irradiation.

3. Results and discussion

3.1. Structural analysis (XRD)

The crystal assembly and phase composition of ZnO nanoparticles were explained by XRD. The XRD spectra for Ca-doped ZnO (1-4%) and pure ZnO are shown in Figure 2. Strong diffraction peaks in all compositions highlight the samples' exceptional crystalline structure, which is consistent with a hexagonal quartzite structure. The synthesized ZnO's strong XRD peak pattern indicates a very accurate single-phase composition, and its noticeably narrow peak breadth indicates improved purity. The structural indexing suggests that the final product exhibit hexagonal crystalline structure (space group P63mc) and no additional contaminants.

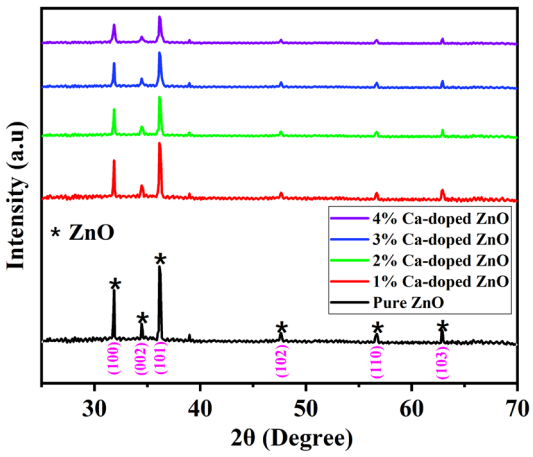

Fig. 2. XRD graph of fabricated hexagonal pure and calcium doped ZnO nanostructure.

The distinctive peaks of the hexagonal wurtzite structure, emerging at diffraction angle (2θ) long miller indices (hkl) are 31.62^0 (100), 34.32^0 (002), 36.16^0 (101), 47.41^0 (102), 56.39^0 (110), 62.64^0 (103), 67.64^0 (112) and 68.61^0 (201) of the bulk ZnO crystal plane, having distinguishing peaks of 31.620 (100), 34.32^0 (002), 36.15^0 (101) and their corresponding intensities correlated with JCPDS card No. 01-079-0208. Due to addition of Ca as dopant, the peaks of the hexagonal wurtzite structure shifted to slightly lower 2θ values contrasted to the peaks of pure ZnO suggesting the proper doping of calcium ion [22, 34-39]. Similar shift of ZnO peaks towards lower angle have been reported by Khataee et al (2017) when incorporated heavier lanthanide ion such as Ho^{+3} (1.015Å)

and Er^{+3} (0.89Å) [40]. The lattice shift, which causes an increase in internal tension inside the source material, is shown by this movement towards lower angles. Dopant was added, and un-indexed peak was not seen. There were not calcium-related peaks seen, confirming that ZnO does not include any other phases [41]. A decrease in crystal size was confirmed by a fall in peak intensity that was proportionate to the dopant concentration [42].

Table 1. Crystallographic features of synthesized pure and Ca-doped ZnO nanomaterial.

Sample	Peak Position ($2\theta^0$) Degree	Peak Position (θ^0) Degree	Peak Position (θ^0) Radian	FWHM ($2\theta^0$) Degree	β Radian	d-spacing (Å)	Scherrer Size (nm)	Micro-strain (ε) ($\times 10^{-3}$)	Dislocation Density (δ) ($\times 10^{14}$ cm^{-2})
Pure ZnO	36.16	18.08	0.3156	0.1982	0.00346	2.4819	42.17	2.6485	0.5624
1% Ca doped ZnO	36.04	18.02	0.3145	0.3445	0.00601	2.4899	24.15	4.6201	1.70
2% Ca doped ZnO	35.94	17.97	0.3137	0.3685	0.00643	2.4966	22.66	4.9576	1.947
3% Ca doped ZnO	35.88	17.94	0.3171	0.4379	0.00764	2.5004	19.07	5.901	2.75
4% Ca doped ZnO	35.73	17.86	0.3117	0.5564	0.00971	2.5111	15.86	7.533	4.444

Calcium doping significantly affected the intensity of diffraction peaks owing to the change in radii between calcium (1.14Å) and zinc (0.88Å). [24]. The enhancement in the amount of calcium in ZnO changes band gap, owing to either surface defect, localized positive charge around zinc or oxygen vacancies within crystal plane which led to decline in crystal size. Calcium ions do not enter the ZnO lattice; rather, they substitute Ca^{2+} ions in the lattice of calcium oxide at the interface with ZnO. Due to its high oxygen affinities and interstitial location, calcium (II) resides in the interstitial site of Ca^{2+}-ZnO [43]. Salveraj et al (2019) has demonstrated the reduction of ZnO under incorporation of higher ionic radius such as Gd^{+3} (0.94Å) [26]. Reduction of crystal size of ZnO under the impact of heavier ions such as Ho^{+3} (1.015Å) and Er^{+3} (0.89Å) [40], Ca^{+2} [44] have been observed in numerous studies.

3.1.1. Scherrer's method (SM)

Crystallite size refers to a nanomaterial's coherent volume for a distinctive diffraction peak. It also pertains to the nanograin size of materials and also their thickness in films [45]. The XRD diffraction peaks were used to control the crystal sizes of both pure and Ca-doped ZnO nanomaterial using the Debye-Scherrer formula using equation 3 [29, 46].

$$D = k\lambda/\beta cos\theta \tag{3}$$

In this formula, β is the full width at half maximum (FWHM), λ is the Cu Source's X-ray wavelength, and θ is the angle of diffraction. The value of Scherer constant (k) is about 0.9.

3.1.2. Scherrer Equation Average Method (SEAM)

The Scherrer relationship in mean form was adopted in every XRD pattern to define the size of crystalline material. Of the ones selected, FWHM was being used to measure full width at half maximum. Similarly, we calculated the average number of crystallites for each β after by the Scherrer equation. To control the average crystalline size of the chosen peaks, we used 45.69 nm, 32.21 nm, 27.51 nm, 25.46 nm, and 24 nm, respectively, based on the instrumentations.

3.1.3. Monshi-Scherrer Method (MSM)

After incorporating changes to the existing Scherrer equation in 2012, Monshi introduced the Monshi Scherrer technique, sometimes referred to as the modified Scherer method (Monshi et al., 2012). This approach may be used to quantify the size of crystallites of zinc oxide nanomaterial. The equation 4 is modified form of equation 3 [47].

$$\beta = \frac{k\lambda}{D} \times \frac{1}{Cos\theta} \tag{4}$$

By taking *ln* on both side, equation 4 modified into equation 5.

$$ln\beta = ln\frac{k\lambda}{D} + ln\frac{1}{Cos\theta} \tag{5}$$

To calculate size of crystallite by Monshi Scherrer approach, plot of $ln\frac{1}{Cos\theta}$ on x-axis against $ln\beta$ on y-axis have been plotted as illustrated in of Figure 3.

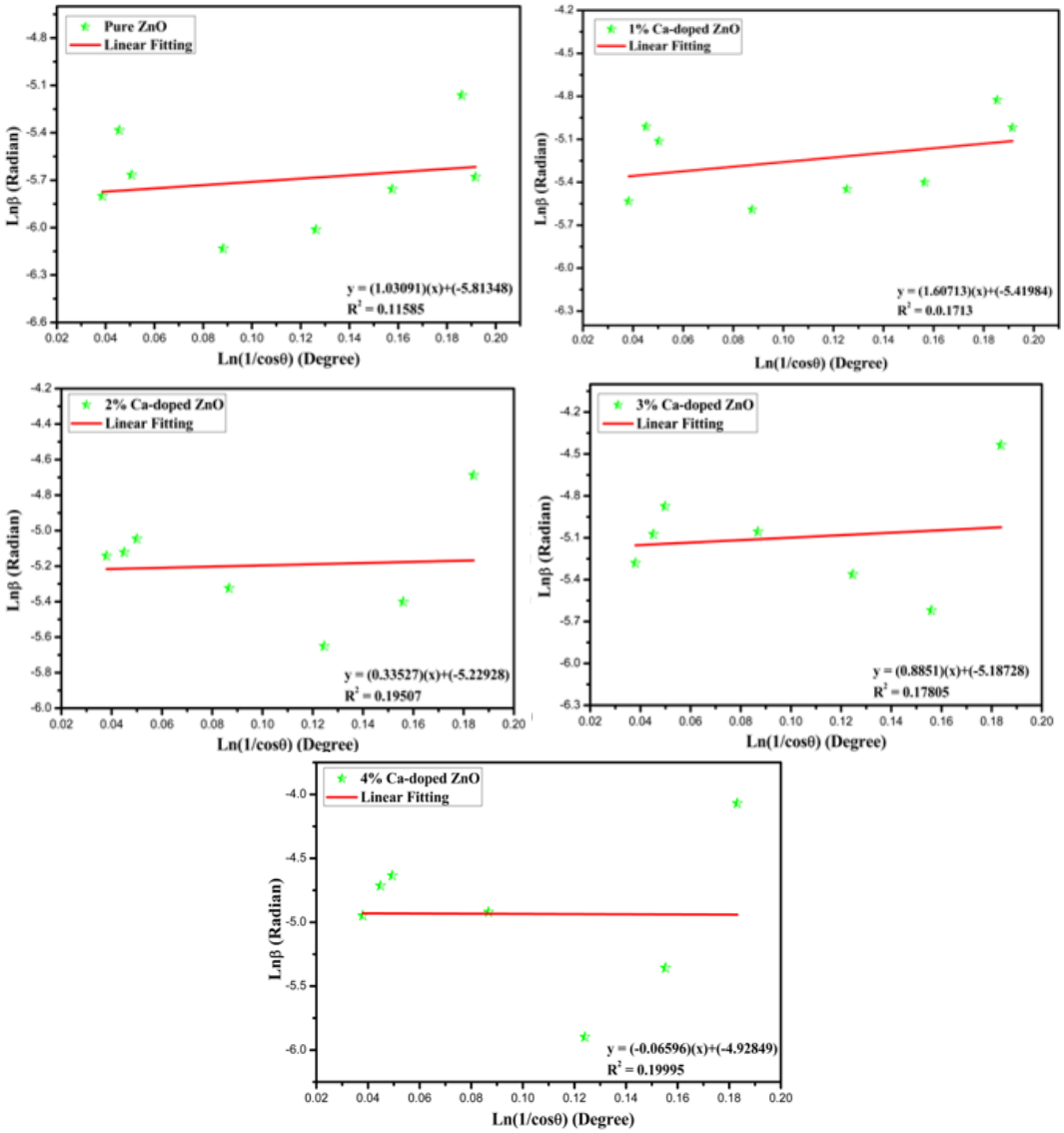

Fig. 3. Monshi-Scherrer method (MSM) linear fit plot for measuring crystallite size of manufactured ZnO nanoparticles.

Comparison of linear fitting of plot against straight line equation (y = mx+c) modified into equation 6.

$$ln\frac{k\lambda}{D} = Intercept \qquad or \qquad \frac{k\lambda}{D\ (nm)} = e^{(Intercept)} \tag{6}$$

The average crystallite size may be determined through an examination at the R^2 values, intercept, and slope. The crystallites' estimated sizes are 46.42 nm, 31.31 nm, 25.88 nm, 24.81 nm, and 19.16 nm, in that order. These numbers are rather close to the typical values for crystalline size. The estimated values of dislocation density (1014 cm^{-2}) are as follows: 0.4641, 1.0198, 1.4929, 1.6237, and 2.7246, in that order.

3.1.4. William-Hall Method (WHM)

The crystalline size of newly synthesised pure and calcium Ca-doped ZnO nanparticles was estimated by the William-Hall (W-H) approach with uniformed deformation model [48, 49]. Since it differs from the Scherrer technique, it effect the size of crystallite on XRD peak expansion, but it also partially represents the influence of strain brought on by XRD peak enlargement [50, 51]. The dependency of 1/cosθ was removed in strain model of William-Hall by doing modification with tanθ [35]. The occurrence of distortion in a powdered crystal sample is called strain. In terms of the idea of strain, the William-Hall model therefore exhibits that the net physical lines broadening (FWHM) of XRD peaks is the result of the combination of strain and size impact according to equation 7 [52, 53].

$$\text{FWHM}_{\text{size}} + \text{FWHM}_{\text{strain}} = \text{FWHM}_{\text{total}} \tag{7}$$

Equation 8 can be used to calculate the strain brought on by the crystal imperfection or distortion [52].

$$\varepsilon = \frac{\beta_{strain}}{4 \times Tan\theta} \tag{8}$$

The equation 9 was produce by combination of equation 3, 7 and 8.

$$\text{FWHM}_{\text{total}} = k\lambda/Dcos\theta + 4\varepsilon(\tan\theta) \tag{9}$$

The equation 10 give rise by rearrangement of equation 9.

$$\text{FWHM}_{\text{total}} \times \text{Cos}\theta = k\lambda/D + \varepsilon(4\sin\theta) \tag{10}$$

To estimate the crystallite size by means of the William-Hall technique, Figure 4 shows a plot of 4Sinθ on the x-axis versus FWHM_total × Cosθ on the y-axis. Equation 11 is the outcome of comparing the linear fitting of the plot with the straight line equation (y=mx+c). Generally speaking, the W-H model is connected to an ideal crystal system, the slope and intercept of the fitted line are thought to represent strain and crystal size.

$$\frac{k\lambda}{D} = Intercept \qquad and \qquad Strain\ (\varepsilon) = Slope \tag{11}$$

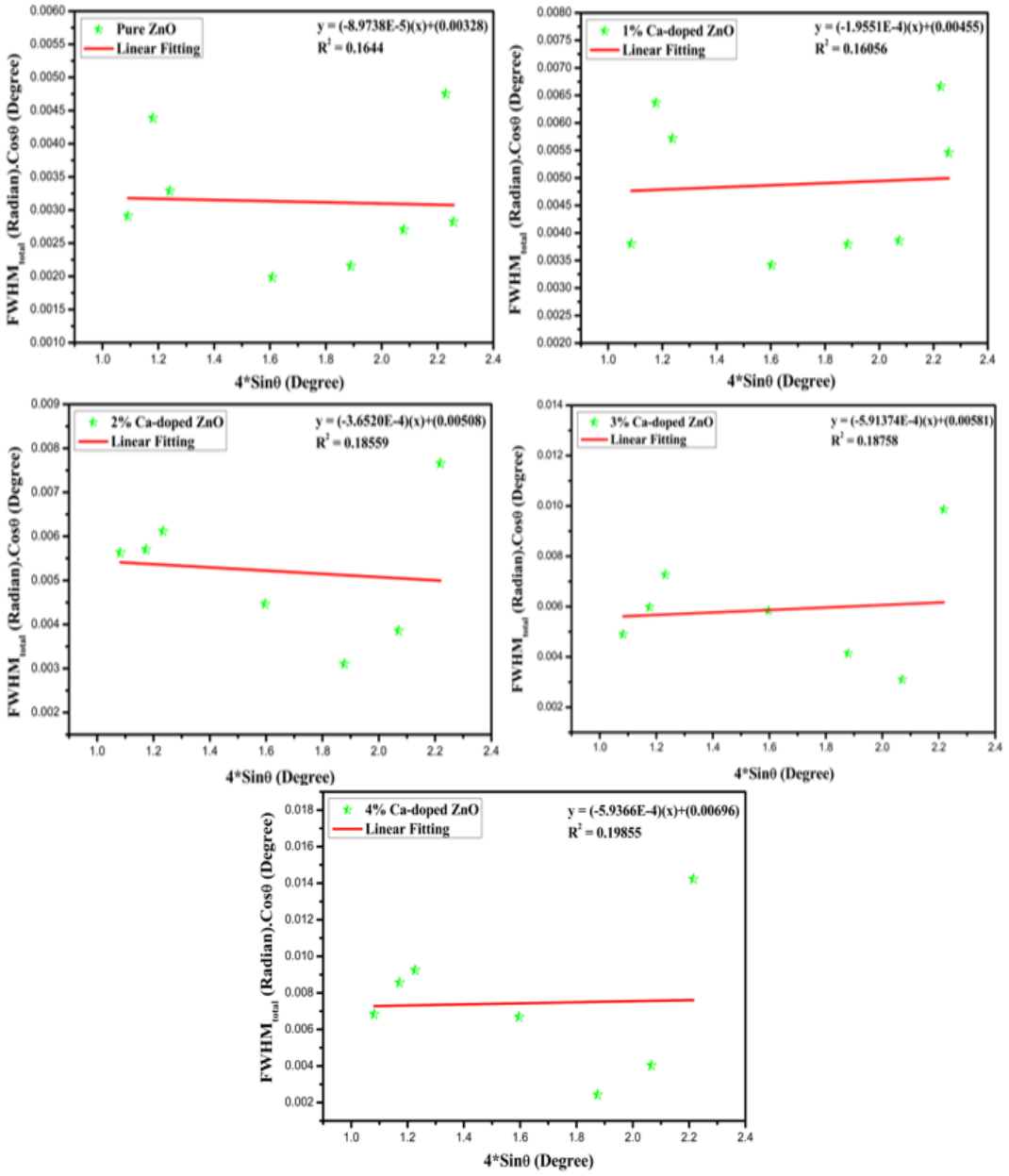

Fig. 4. Linear fit plot of W-H method for measuring crystalline size of fabricated ZnO.

The W-H plot was used to calculate crystallite size as 42.27 nm, 30.47 nm, 27.29 nm, 23.86 nm, and 19.92 nm while strain (ε) estimated to be $-0.0897E^{-3}$, $-0.1955E^{-3}$, $-0.3652E^{-3}$, $-0.5194E^{-3}$, and -0.5936 respectively. Positive strain (ε) values agree with tensile strain whilst negative values (ε) agree with compressive strain [54]. The dislocation density (δ) (10^{14} cm^{-2}) is intended to be 0.5596, 1.077, 1.342, 1.756, and 2.52 respectively.

3.1.5. Size-strain method (SSM)

The size-strain plot approach uses the Lorentz and Gaussian functions for size and strain broadening as βL and βG study (Equation 12) [55]. The size-strain plot is mainly explain the isotropic crystal system as well as long angle reflection [50, 56].

$$\beta_{hkl} = \beta_L + \beta_G \tag{12}$$

$$(d\beta Cos\theta)^2 = \frac{k\lambda}{D} \times (d^2\beta Cos\theta) + \frac{\varepsilon^2}{4} \tag{13}$$

The d-spacing measures hkl planes inside the hexagonal structure of zinc oxide nanomaterials and is determined using equation 13. Figure 5 shows a plot of $(d\beta Cos\theta)^2$ on the y-axis vs $(d^2\beta Cos\theta)$ on the x-axis. The intercept $(\varepsilon^2/4)$ and slope (k/D) values from this figure determine the crystallite size and inherent strain of hexagonal zinc based nanomaterial. The calculated normal crystallite sizes are 33.46 nm, 22.47 nm, 21.43 nm, 19.86 nm, and 15.94 nm, respectively. Alongside, the inherent strain values for pure and Ca-doped ZnO have not been found. Particularly, the scientific calculation of intrinsic strain for the material is rendered impossible due to the negative intercept values. However, the dislocation density value (1014) obtained from this model produces 0.8933, 1.9802, 2.1774, 2.5342, and 3.9372 for the correspondin material.

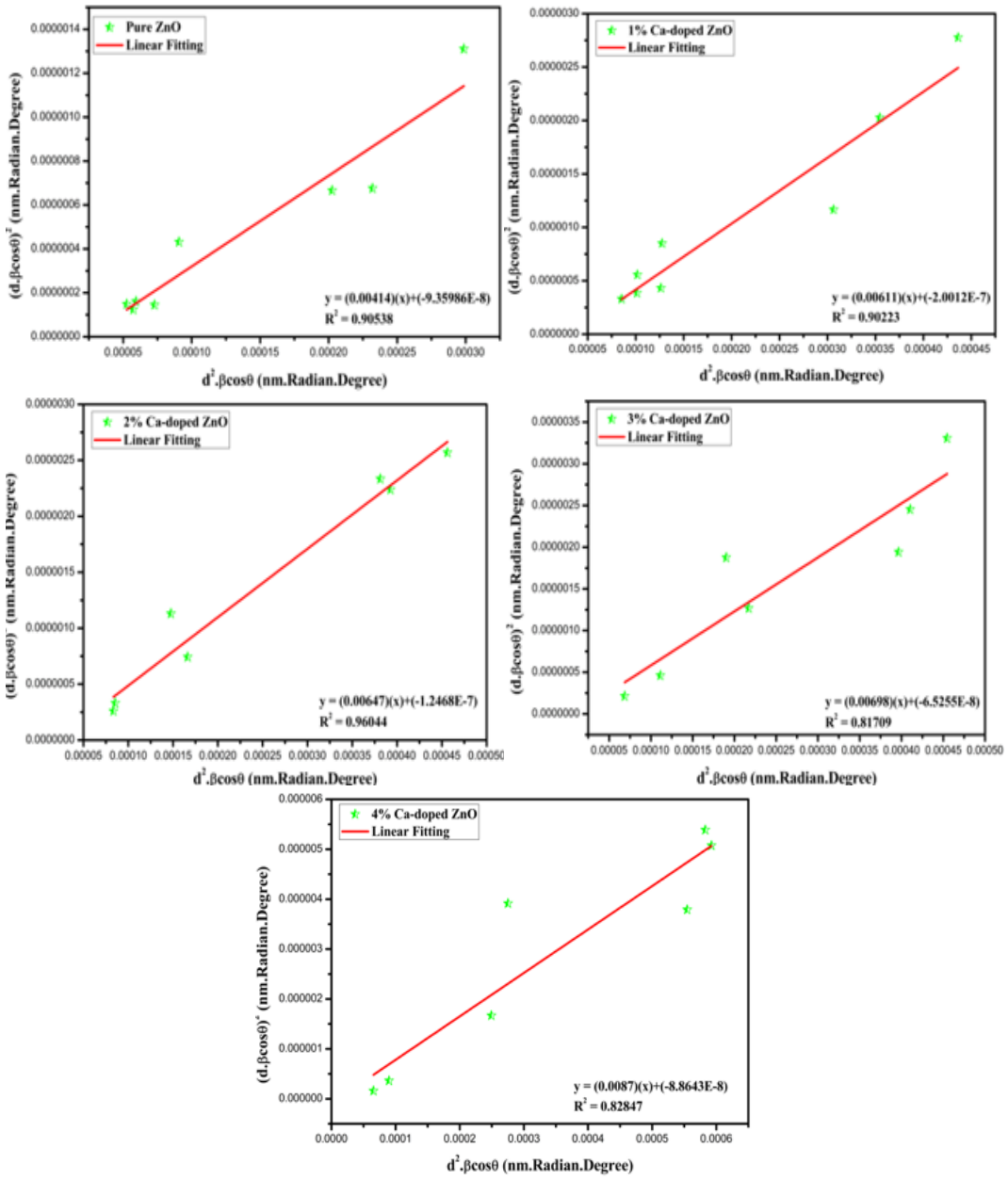

Fig. 5. Size-Strain plot with a linear fit for determining the crystalline size of ZnO nanomaterial.

3.1.6. Halder-Wagner Model (HWM)

The Halder-Wagner model's requirement for crystalline size is based on the observation that the XRD peak profile's size enlargement depends on a symmetric Voigt function rather than a Lorentzian or Gaussian function. To study this problem, the Halder-Wagner method proposes the following equation 14 for the Voigt function [50].

$$\beta^2_{hkl} = \beta_L \times \beta_{hkl} + \beta^2_G \quad (14)$$

The full-width, half-maximum Lorentzian and Gaussian functions are denoted by the functions βL and βG. With reduced diffraction peak overlap and a greater focus on the peaks at low and medium angles, the Halder-Wagner approach provides benefits over other techniques. The Halder-Wagner approach's computational equation is shown in equation 15.

$$\left(\frac{\beta^*}{d^*}\right)^2 = \frac{k\beta^*}{D(d^*)^2} + (2\varepsilon)^2 \quad (15)$$

where

$$\beta^* = \frac{\beta Cos\theta}{\lambda} \quad \text{and} \quad d^* = \frac{2dSin\theta}{\lambda}$$

The equation 15 rearranged and produce equation 16.

Linear fitting plot of equation 16 was drawn by taking $\left(\frac{\beta}{Tan\theta}\right)^2$ on y-axis against $\frac{\beta Cos\theta}{(Sin\theta)^2}$ on x-axis which can be seen in Figure 6. K$_\epsilon$/D gives the slope, and 16$\epsilon^{\wedge 2}$ gives the intercept value, which may be utilized to calculate the dislocation density, crystalline size, and strain. The measured crystalline sizes are 33.49 nm, 22.47 nm, 21.39 nm, 20.12 nm, and 15.93 nm; however, the sample strain could not be quantitatively determined because of the negative intercept value. Additionally, the synthesized sample's dislocation density (H1014) is calculated to be 0.8915, 1.9802, 2.1842, 2. 4693, and 3.9371, in that order.

$$\left(\frac{\beta}{Tan\theta}\right)^2 = \frac{k\lambda}{D} \times \frac{\beta Cos\theta}{(Sin\theta)^2} + 16\varepsilon^2 \quad (16)$$

Linear fitting plot of equation 16 was plotted by taking $\left(\frac{\beta}{Tan\theta}\right)^2$ on y-axis against $\frac{\beta Cos\theta}{(Sin\theta)^2}$ on x-axis which shown in Figure 6. K$_\epsilon$/D gives the slope, and 16$\epsilon^{\wedge 2}$ gives the intercept value, which may be used to calculate the strain, crystalline size, and dislocation density. The measured crystalline sizes are 33.49 nm, 22.47 nm, 21.39 nm, 20.12 nm, and 15.93 nm; however, the sample strain could not be quantitatively determined because of the negative intercept value. Additionally, the synthesized sample's dislocation density (H1014) is calculated to be 0.8915, 1.9802, 2.1842, 2. 4693, and 3.9371, in that order.

The interplaner spacing (d) is calculated by Bragg equation although other lattice constraints and volume of hexagonal structured pure NPs and calcium doped zinc oxide was calculated by equation 17-19 mention in documented studies [22, 39, 57-59].

$$d_{hkl} = n\lambda/2\, Sin\theta_{hkl} \quad (17)$$

$$\frac{1}{d^2_{hkl}} = \frac{4}{3}\left(\frac{h^2+hk+k^2}{a^2}\right) + \frac{l^2}{c^2} \quad (18)$$

$$V = \frac{\sqrt{3}a^2c}{2} = 0.866a^2c \quad (19)$$

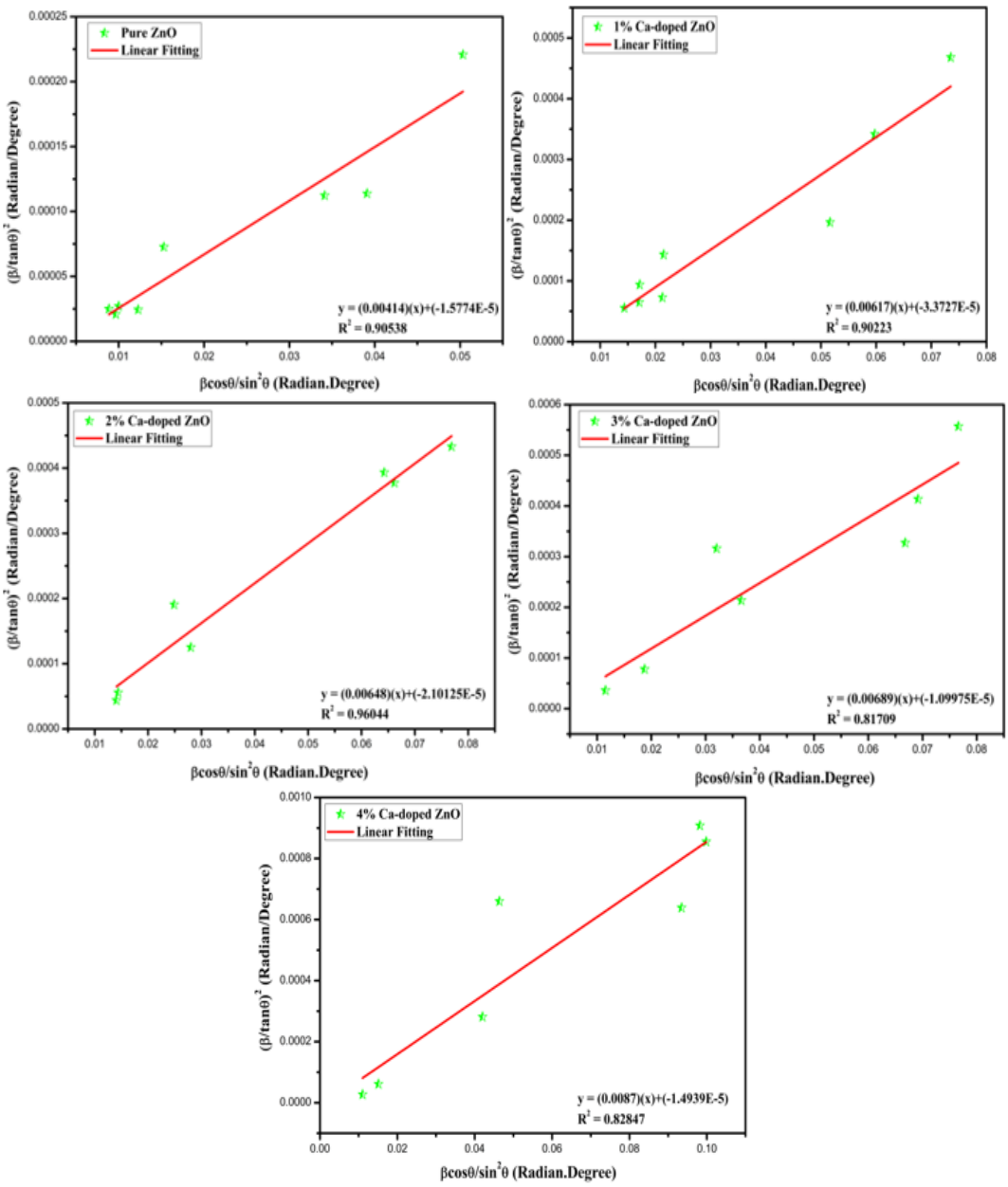

Fig. 6. Estimating the crystalline size of ZnO nanomaterial using a linear fit plot of the Halder-Wagner plot method.

The computed lattice parameters of pure zinc oxide (Table 2) are as follows: a = 3.2627 Å, b = 3.2627 Å, c = 5.2218 Å, γ= 120°, and V = 48.21 and related to documented studies [22, 36, 37, 58-61]. The difference of crystalline size and lattice constants and are in agreement to Vegard's law. Using obtained X-ray data, the crystallite density (g/cm3) may be calculated using equation 20, which is documented in literature [33, 62] where, in accordance with equation 19, V stands for the volume of the material's unit cell under examination, which is hexagonal. Since a hexagonal crystal structure has two molecules in its geometry according to the JCPD card and NA is an element of the Avogadro number having value of $6.02*10^{23}$ mol^{-1}.

$$\rho_x = \frac{A}{N_A \times V} \quad or \quad \rho_{ZnO} = \frac{2 \times Molecular\ weight}{N_A \times \frac{\sqrt{3}a^2 c}{2}} \tag{20}$$

Table 2. The comparison of Lattice constraints of JCPDS card and experimental synthesized nanomaterials.

Lattice Parameters (Å)	a (Å)	b (Å)	c (Å)	γ^0	Volume of unit cell V $(Å)^3$	Crystal density ρ_x (g/cm^3)	Specific Surface Area (m^2/g)
JCPDS value (01-080-1916)	3.2648	3.2648	5.2194	120	48.18	5.61	-
Pure ZnO	3.2627	3.2627	5.2218	120	48.14	5.618	0.023426
1% Ca doped ZnO	3.2274	3.2274	5.1859	120	46.78	5.776	0.032250
2% Ca doped ZnO	3.2151	3.2151	5.2203	120	46.73	5.782	0.037720
3% Ca doped ZnO	3.2148	3.2148	5.1599	120	46.05	5.862	0.040201
4% Ca doped ZnO	3.2085	3.2085	5.1476	120	45.89	5.899	0.042380

The modification of lattice properties in crystalline material was known as the micro-strain or local strain [63]. Using equations 21 and 22 [33, 64], the macro-strain and dislocation density (δ) calculated. Table 1 presents the attained values of micro strain and dislocation density of produced NPS for a certain plane. These values were impacted by both promiscuous grain dispersion and atom replacement or relocation.

$$\varepsilon = \beta/4\tan\theta \tag{21}$$

$$\delta = 1/D^2 \tag{22}$$

Scherrer equation 3's average particle size yields the SSA value indirectly. The SSA value has a significant influence on the features of NPs, and the manner that the surrounding medium interacts with the nanoparticles is also very influential. Equation 23 may be used to get the specific surface area of an presumed spherical particle by using its density (ρ-x) and average particle size (D) [65].

$$SSA = \frac{6}{D \times \rho} \tag{23}$$

3.2. Morphological and compositional investigation (SEM, EDX)

The morphological characteristics of the synthesized nanomaterials, which included pure ZnO and Ca-doped ZnO at different doping percentages (1%, 2%, 3%, and 4%), were examined by SEM analysis. The high resolution surface morphology of the nanomaterials was shown by the SEM micrographs in Figure 7 (a-d). Smooth surfaces and apparent grain boundaries defined the uniformly packed structure of the pure ZnO nanoparticles. There were noticeable morphological alterations as the calcium doping % increased. The nanoparticles showed small differences in grain size and distribution and minimal surface feature changes as compared to pure ZnO at lower doping concentrations (1% and 2%). On the other side, the SEM images of the ZnO nanoparticles with 3% Ca doped showed notable morphological modifications that suggested enhanced photocatalytic activity. These nanoparticles seemed to have a more porous structure and rougher surfaces, which suggests that they had greater surface area and better light-absorbing capabilities. At this optimal concentration, the Ca dopant seems to encourage the creation of distinctive nanostructures, which may have an impact on the formation and effective application of photoinduced charge carriers. However, the doping percentage up to 4% led to the formation of irregularly shaped agglomerated nanoparticles and a loss in surface homogeneity.

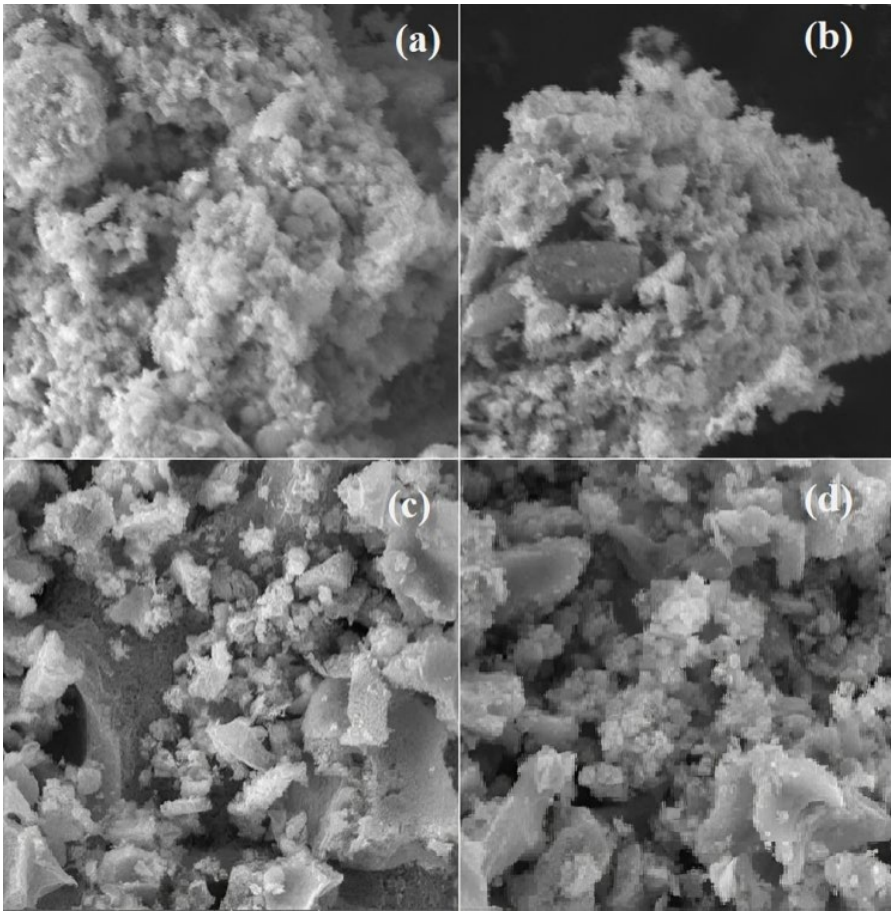

Fig. 7. SEM of metallic NP (a) Pure ZnO, (b) 1% Ca doped ZnO, (c) 2% Ca doped ZnO (d) 3% Ca doped ZnO.

EDX technique is employed to study the elemental conformation of a material. EDX provides additional information about elemental composition [66]. The fundamental composition of synthesized pure and doped metal oxide nanostructures was examined. The EDX spectra of pure and 3% Ca doped ZnO NPs made by means of the sol-gel method are shown in Figures 8(a-b), respectively. These spectra verified the distribution of Ca on ZnO's surface. The EDX spectra of pure ZnO depicted the presence of Zn and O peak that confirm the synthesis of pure metal oxides without any impurity. The spectra of doped materials depicted an additional peak of Ca with immense %age that guarantee the doping of calcium in pure ZnO nanomaterials.

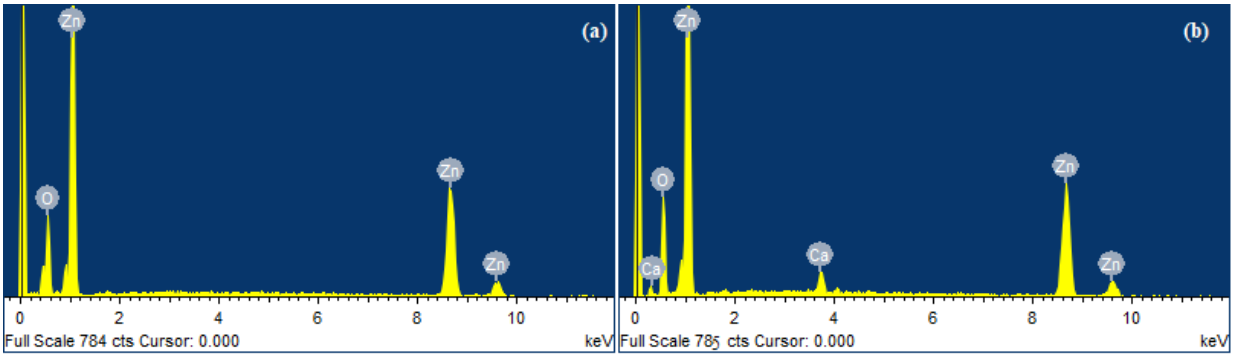

Fig. 8. EDX spectrum of (a) pure and (b) 3% Ca doped Zinc Oxide.

3.3. Optical and Luminescence Properties (UV, PL)

The UV-Vis technique was utilized to explore the optical properties of ZnO nanoparticles. Figure 9 illustrates absorption bands corresponding to different compositions: pure ZnO, as well as ZnO doped with 1%, 2%, 3%, and 4% Ca. The samples displayed unique absorption peaks at specific wavelengths: 360 nm for pure ZnO nanoparticles, 370 nm for ZnO doped with 1% Ca, 375 nm for 2% Ca doping, 375 nm for 3% Ca doping, and 381 nm for 4% Ca doping. The observed slight shifts in the absorption bands were attributed to the presence of the dopant material. Notably, a more significant shift in the absorption bands was observed as the dopant material concentration increase [67]. This change was ascribed to the higher dopant concentration's improved interaction potential with UV-Vis radiation of the nanomaterials [68]. Consequently, these doped nanoparticles exhibit potential for use in photocatalytic dye degradation, particularly when exposed to sunlight [31, 69].

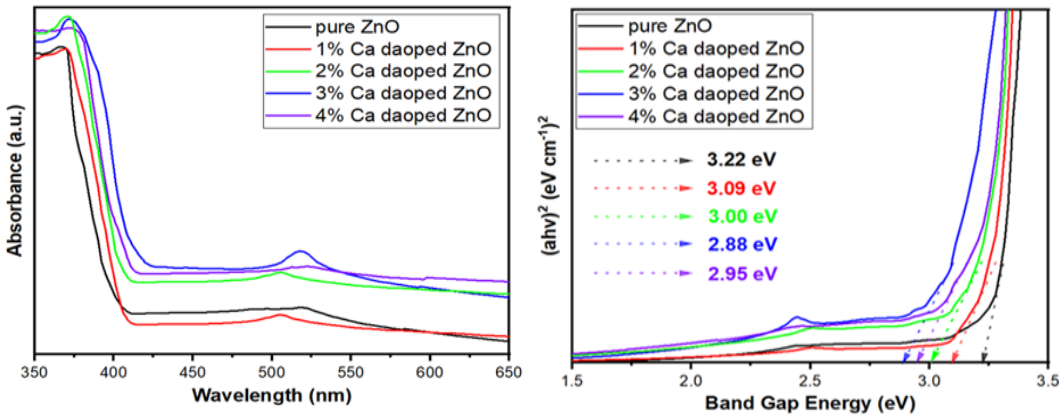

Fig. 9. Absorption spectra and Tauc plot of pure and Ca-doped ZnO nanostructure.

The energy gap has been pushed nearer the visible area by doping. Figure 9 illustrates the estimation of the direct energy gap of pure and doped nanomaterials using the Tauc plot relation from equation 24 [33, 69]. Direct bandgap of pure and calcium doped from this relation is 3.22 eV, 3.09eV, 3.00 eV, 2.88 eV, 2.95 eV respectively.

$$ahv = (hv - Eg)^2 \tag{24}$$

These findings indicate that adjusting the dopant concentration reduces the band gap towards the visible region when compared to pure samples. This adjustment is highly favourable for photo-catalytic applications. The band gap was decreased by calcium doping from 3.22 eV to 2.88 eV. The photoluminescence (PL) spectra in Figure 10 illustrated the examination of the prepared NPs.

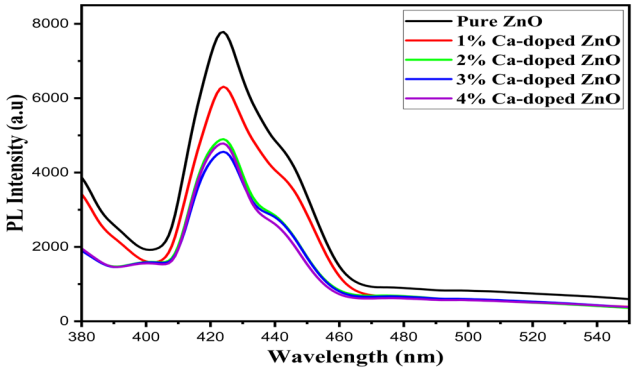

Fig. 10. Photoluminescence (PL) spectra of nanostructure zinc oxide.

PL spectroscopy was employed for the assessment of optical features and the effectiveness of electron-hole recombination. The photoluminescence (PL) emission spectra for pure and Ca-doped ZnO samples are shown in Figure 10, with the results spanning from 380 nm to 540 nm. The most prominent peak at 421 nm is the exposition of the near-band-edge emission of ZnO [70]. Interestingly, CaO addition can introduce the band gap shift itself, which is the opposite effect [21]. Incorporation of Ca-dopant ions in the bandgap creates some levels of energy, which may seem responsible for the changed peak position [13]. It was reported that the strength of a peak was limited as the concentration of calcium dopant rised. The beginnings of intensity at the peak were associated with changes in ionic radii arises from the incorporation of Ca dopant. Furthermore, doping the compound causes a charging carrier's separation that is considerably pronounced, which enhances photocatalysis effectiveness. This enhancement can be due to the decrease in electron-hole pair recombination events, which eventually is the main factor affecting the process performance [28].

4. Photocatalytic wastewater treatment

4.1. Effect of contact time

In order to test the photocatalytic potential of ZnO NPs and Ca-doped ZnO NPs, the degradation of dyes was performed. A temperature control system was established for the reaction, and a 300W visible-UV lamp, which has wavelengths longer than 420 nm, was used as the photocatalytic material to degrade organic contaminants in the reactor. The model pollutant at a 25 ppm concentration was next placed in the absence of light with the solution under investigation.

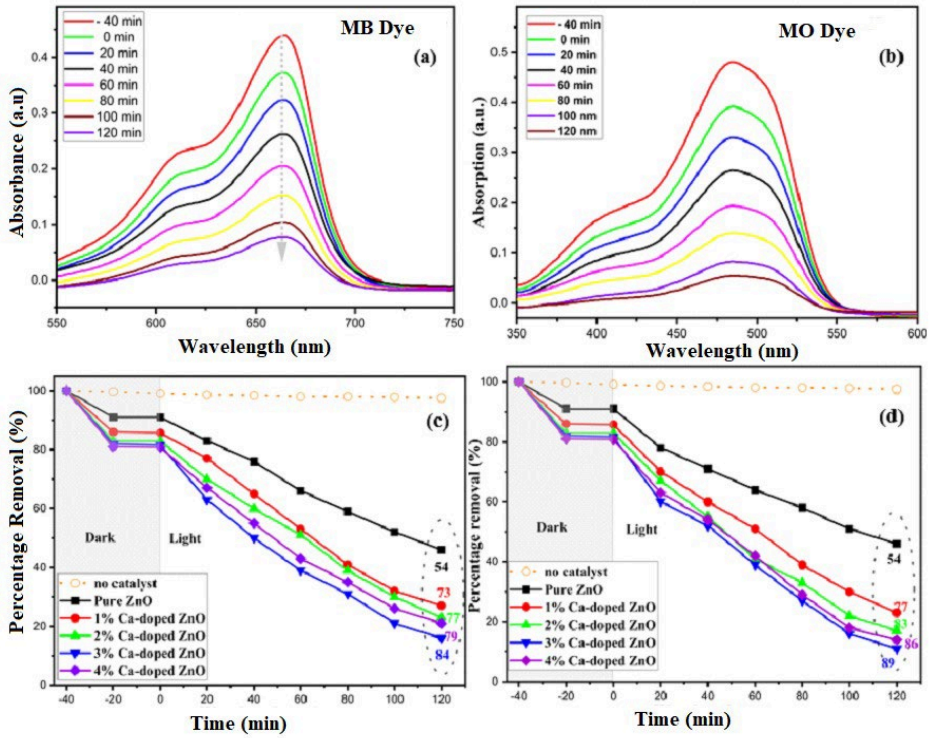

Fig. 11. The suppression of characteristic absorption peaks indicative of dye degradation (a-b), while the percentage of dye removal facilitated by the fabricated nano-photocatalysts (c-d).

Alternately, UV-visible absorption spectroscopy was employed to confirm this solution, and the peak absorption value of the MO was 464 nm, whereas in the case of the MB, the peak absorption value was 665 nm [71]. The amount of 100 mg of NPs was added to mixture [72]. The 40 minutes was given to performed the reaction process. The complete reaction process was completed in a dark condition to maintain the phenomena of absorption and adsorption. The entire reaction took place in the corresponding lab, at room temperature, and under normal conditions. Subsequently, for 120

minutes, the suspension was exposed to light. UV-visible spectroscopy was utlized to track the changes at intervals of 20 minutes [69]. The degradation of the dyes, as illustrated in Figure 11 (a) and (b) was indicated by a decrease in the strength of the distinctive absorption peaks. This process was repeated for every sample concerning both MB and MO dyes. During the complete experiment, optimized conditions were espoused for factors such as pH, catalyst dose and temperature.

The degradation percentage of dye calculated using equation 25 [33, 37, 69].

$$\%\, removal = {(C_t - C_o)}/{C_0} \times 100 \tag{25}$$

The degradation percentages of MB were 54%, 73%, 77%, 84%, and 79% respectively for concentrations of 0%, 1%, 2%, 3%, and 4% of Ca-doped ZnO as illustrated in figure 11 (c). This trend is reflected in the breakdown of MO, which exhibited degradation percentages of 54%, 77%, 83%, 89%, and 86% respectively with the concentration of 0%, 1%, 2%, 3%, and 4% Ca-doped ZnO as depicted in figure 11 (d). These results significantly highlight the sharp photocatalytic efficacy of ZnO owing to the value of dopant concentration. The increase of dopant concentration improved the photocatalytic potential by dropping the rate as photogenerated electron-hole pairs recombine. Furthermore, various studies using UV-Vis spectroscopy have shown that the addition of Ca implied in the reduction of ZnO band gap. The decrease in the band gap facilitates the proficient utilization of visible light, adding another dimension to the heightened photocatalytic activity. Additionally, XRD studies emphasized the impact of doping on particle size reduction, consequently amplifying the effctive surface area. The expanded active surface area facilitates the adhesion of a greater number of pollutant molecules to the catalytic surface area, thereby promoting the photocatalytic reaction. The photocatalytic effectiveness was raised from 54 to 84% for 3% calcium doped ZnO sample because an upsurge in dopant concentration enhances the active surface area, decreases the band gap, recombination rate, and particle size. When 4% Ca is doped with ZnO, due to Burstein Moss result [73], band gap energy is improved which could be the reason for decrease in catalytic efficiency. It indicates that 3% Ca doped is optimal for ZnO and that further raising the dopant concentration could have a negative impact on efficiency.

4.2. Kinetic modelling

Photocatalysis can exhibit pseudo-first-order behavior under different conditions. Various factors can impact the rate of reaction over time and depart the process from rigid pseudo-first-order kinetics, equations 26 and 27 of the Langmuir-Hinshelwood (L-H) model must be used to study the photocatalytic reaction rate constant at the solid-liquid interface [33].

$$\frac{dC}{dt} = -kC \tag{26}$$

$$-ln\frac{C_0}{C_t} = kt \tag{27}$$

The rate constants for the degradation of dyes are shown in Figure 12(a) and (b), respectively. For every linear fitting, the R2 value is more than 0.95, suggesting a stronger correlation between the L-H model. It is clear from the calculations that the photocatalyst has slightly higher tendency for degrading MO as compared to MB. The higher rate constant in both cases were given by the 3% Ca-doped ZnO samples. The rate constant is increased by 2.11 and 2.02 times respectively for MO and MB removal in contrast to pure samples.

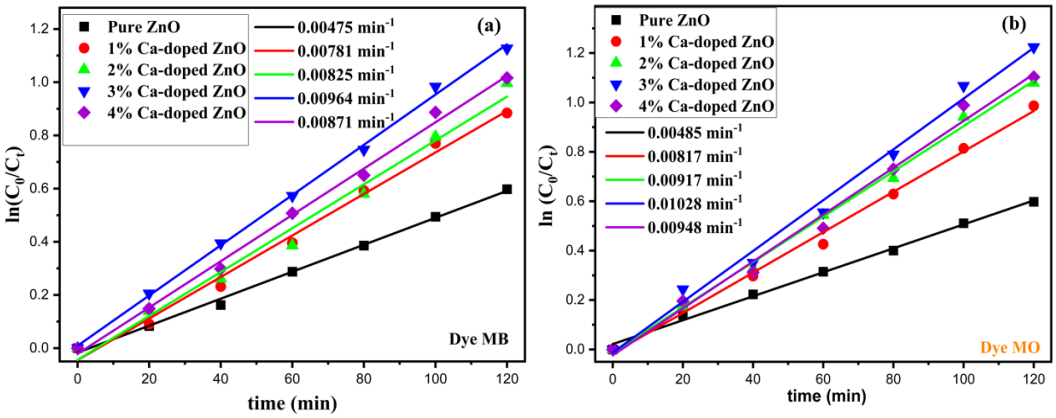

Fig. 12. Representation of rate constant for the degradation of MO and MB dye in synthesized nano-material.

4.3. Effect of pH

The pH plays major role in surface charge properties and the efficacy of contaminant adsorption on the photo-catalyst. The effects of 3% Ca-doped zinc oxide on methyl orange were examined within a pH range of 3-10. The pH of the combination was different before to radiation and was not maintained at the same level during the process. Figure 13(a) displays the percentage of dye degradation in the 3% Ca-doped zinc oxide at various pH levels. The ZnO photocatalyst's (PZC 9) isoelectric point (IEP) and surface characteristics are the sources of this variability [74], as well as the charge properties of dye molecules in aqueous media. ZnO powder has an isoelectric point (IEP) of around pH 8.60/9 [61]. ZnO surfaces carry a positive charge in acidic and neutral media, whereas they become negatively charged in highly alkaline solutions [38, 75]. This implies that the surface of photocatalyst is protonated when pH<pH pzc leading to greater adsorption of anionic dye and deprotonation will occur when pH>pH pzc causing electrostatic repulsion of photocatalyst with hydroxyl ion. MO being anionic dye will preferentially adsorbed on fabricated ZnO at pH <9 due to electrostatic attraction [76]. Performance of degradation has been improved with the change of pH, with highest 93% exhibition of deterioration at pH 8 which has declined further with the pH increased. The maximum degradation action at alkaline media mainly attributed to facilitation of methyl orange (positively charged) adsorption on photocatalyst (negatively charged) due to electrostatic interaction [31, 77]. The deterioration in photocatalytic efficiency in acidic pH correlated to lower dissolution of zinc oxide NPs [28]. This implies that lesser activity of ZnO at acidic media is due to higher instability of ZnO and formation of Zn^{+2}. Similar case of fabricated AgBr-ZnO against anionic dye BPB and EY have been stated by Ahmed et al., (2018) in which greatest activity was observed at pH 8 and declined at higher pH=10 [76]. Toloman et al (2021) have demonstrated the greater efficiency of Cu-doped ZnO MWCNT nanocomposites at pH 6 against RhB, Phenol, and OTC contaminants which declined at higher pH [78]. Moreover, AgIO4/ZnO against RhB dye have demonstrated similar effect [36]. Numerous documented research indicating greater rate of degradation of several cationic dye at larger pH through modified zinc oxide, have been published [36, 61, 76, 79].

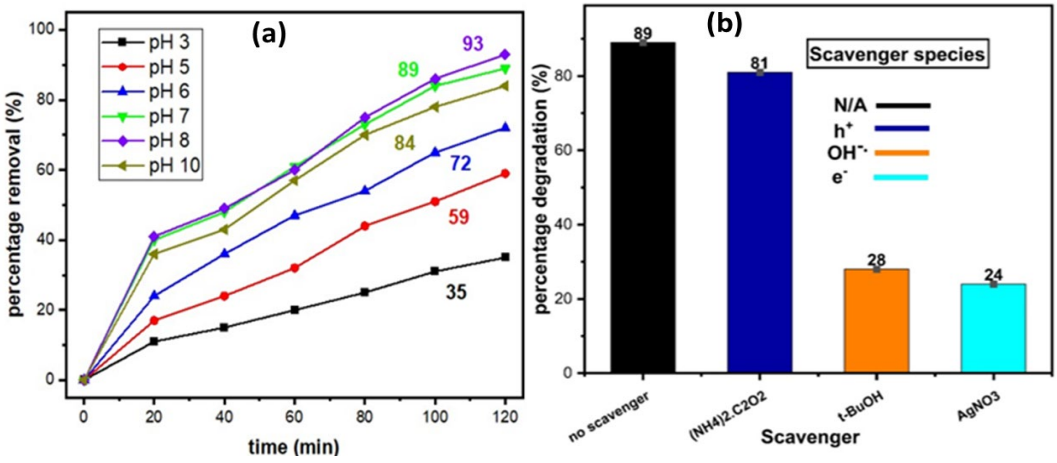

Fig. 13. (a) Influence of pH on catalytic functioning (b) Scavenger experiment confirming contribution of hydroxyl radicals in photocatalytic reaction.

4.4. Scavenger experiment and reusability

Photocatalytic reaction produces numerous species i.e., holes (h^+), free e^-, and oxidation radicals. The trapping of radical investigation Figure13(b) by means of 1mM of various reagents like $(NH_4)_2.C_2O_2$, t-butanol and silver nitrate, on the best sample have been conducted to confirm solely responsible active species for dye degradation [33, 80]. Higher disintegration rate has been observed for scavenger free system. Silver nitrate and tertiary butanol addition has substantially declined the dye degradation by extinguishing hydroxyl and electrons produced during reaction, representing the influence of hydroxyl and electron in the process of dye degradation [23, 33, 38]. The addition of $(NH_4)_2.C_2O_2$ trap the electrons and hydroxyl radicals. Reusability experiments were carried using the best samples i.e. 3% Ca doped ZnO over six cycles to check the stability of the catalyst in light. The results shown in Figure 14 have revealed that minor significant change in the activity of synthesized photocatalyst has taken place over the many cycles, affirming the high photo-stability of material [36, 37, 39, 61]. An experiment was conducted to assess the photo-stability of 3% Ca-doped Zinc Oxide through six cycles of reuse. The degradation value decreased from 89.11% to 81.33% after six cycles, indicating improved stability and remarkable photocatalytic activity of the material.

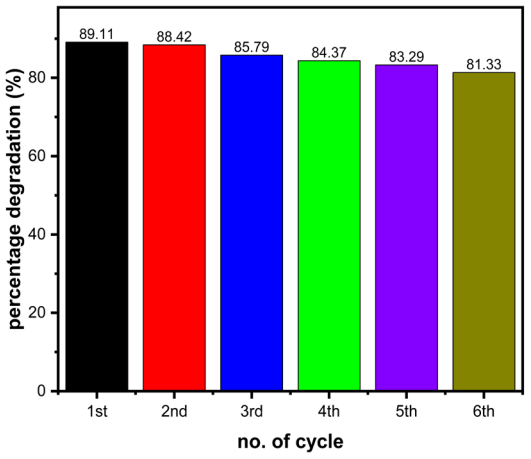

Fig. 14. Reusability experiment to check the photo-stability of the 3% Ca-doped Zinc Oxide over six cycles.

4.5. Mechanistic path for photo-degradation of dyes

The proposed protocol for the photocatalytic decomposition of MO is illustrated in Figure 15. When the material is photoexcited, it triggers the photocatalytic degradation of the dye in the attendance of a catalyst, leading to the generation of electron-hole pairs, as depicted in equations 28-33. A specific part of methylene orange dye combine with photogenerated carriers, while remaining move towards catalyst surface, where hole acts as powerful oxidant and electron as reductant [28, 81]. By using hole as a reactive intermediate in hydroxyl ion reactions or H_2O breakdown, hydroxyl radicals are created, which causes the dye to breakdown [82]. Moreover, when a dye molecule shares electrons with the conduction band, a dye radical is formed that is eventually depleted. The dissociation and the association of photogenerated charge carriers are possible routes, and significant photocatalytic activity may be achieved [32]. Scavenger studies proving hydroxyl and oxygen radicals were the primary reactive radicals for the photodegradation of methylene blue dye support this hypothesis. The comparative reported investigations of the ZnO nanoparticles doped by Ca are presented in Table 3.

$$ZnO + hv \rightarrow ZnO(h^{+}) + ZnO(e^{-}) \quad (28)$$

$$\text{Electron} + Ca^{+2} \rightarrow Ca^{+1} \quad (29)$$

$$h^{+} + H_2O/OH^{-} \rightarrow {}^{\bullet}OH \quad (30)$$

$$Ca^{+1} + O_2 \rightarrow {}^{\bullet}O_2^{-} + Ca^{+2} \quad (31)$$

$$O^{\bullet}{}_2 + 2H^{+} \rightarrow 2OH^{\bullet} \quad (32)$$

$$O^{\bullet}{}_2 + 2OH^{\bullet} + \text{dye} \rightarrow \text{Non} - \text{Pollutant by-product} \quad (33)$$

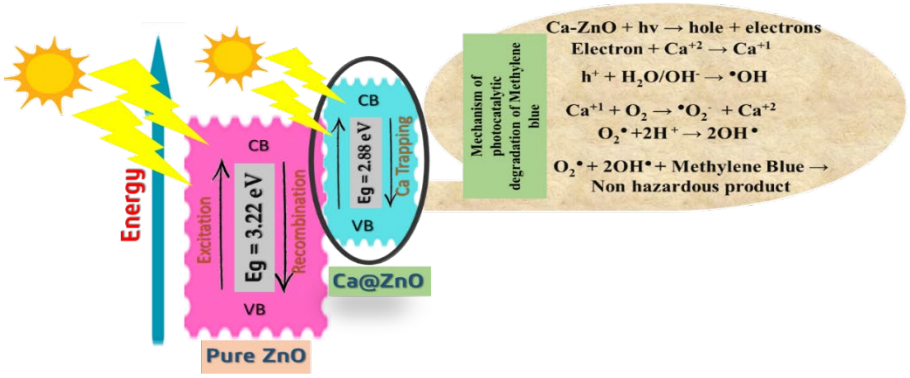

Fig. 15. Proposed reaction mechanism of methylene orange degradation via free radical reaction to dye solution.

Table 3. Comparative studies of synthesized photocatalyst with documented photocatalyst.

Photocatalyst	Dye	Irradiation Source	Photocatalyst (mg)	Time (min)	Degradation (%)	References
$AgIO_4$/ ZnO	RhB	Hg lamp	100	120	81	[36]
Hf doped ZnO	MB	Sunlight	250	120	85	[60]
Bi2MoO6/ZnO	MB	UV-Vis	-	150	90	[83]
N- doped ZnO	R6G	Xe lamp	10	160	85	[84]
Pt- doped ZnO	MB	Hg lamp	5	120	70-75	[85]
Bi-doped ZnO	CR	UV lamp	100	60	85	[86]
Cu-doped ZnO	RhB	Halogen Lamp	10	240	<80	[78]
Mn-doped ZnO	RhB	UV light	100	300	75.55	[32]
Ag-ZnO	AY99	UV lamp	100-1000	90	<88	[37]
Ni-doped ZnO	RhB	UV light	100	300	68.52	[32]
Sn:Cu:ZnO	MB	Halogen Lamp	100	180	99	[39]
Ag-doped ZnO	RhB	UV light	100	300	93.82	[32]
Cu-ZnO	MO	UV light	50	180	99	[23]
Cu-doped ZnO	RhB	UV light	100	300	79.37	[32]
Mg-ZnO	CR	Sunlight	50	120	57	[87]
Cd-doped ZnO	RhB	UV light	100	300	76.99	[32]
ZnO	MB	Sunlight	100	150	<88	[88]
Ca-doped ZnO	MO	Sunlight	10	129	89	Our work

5. Conclusions

The pure and Ca-doped ZnO NPs were easily prepared by sol-gel method. A combination of numerous characterization techniques was applied to define the optical, structural, and morphological properties of the nanomaterial fabricated, namely UV-visible spectroscopy, photoluminescence analysis, XRD, EDX and SEM. The XRD study has clearly confirmed the hexagonal crystalline structure of the synthesized materials. The effect of the dopant concentration on the band gap of ZnO was distinctly observed via UV-visible analysis. Initially, the band gap showed a reducing trend as the dopant concentration just increased up to 3%. Subsequent increments in the dopant concentration led to a reduction in the band gap, attributed to the Burstein-Moss effect. Furthermore, the PL analysis has revealed that the rate of recombination of electron-hole pairs was suppressed in the doped samples. Remarkably, among the doped samples, the 3% doping level demonstrated the most noteworthy photocatalytic degradation efficiency. This specific sample achieved degradation rates of up to 89% for MO and 84% for MB. The highest degradation efficiency of the 3% doped sample can be attributed to its minimal band gap, which enhances absorption in the visible spectrum. Moreover, the size of the doped samples particle was smaller than that of the pure sample, resulting in an improved specific surface area for the material. This larger surface area delicate the likelihood of dye molecule attachment to the catalyst's surface, thereby augmenting the degradation process.

Acknowledgements

The authors extend their appreciation to Taif University, Saudi Arabia, for supporting this work through project number (TU-DSPP-2024-91).

Funding

This research was funded by Taif University, Saudi Arabia, Project No. (TU-DSPP-2024-91).

Data Availability

The data will be available on request.

Conflict of interest

The authors have no conflict of interest.

References

[1] L. Schweitzer, J. Noblet, Green chemistry, Elsevier, 2018, pp. 261-290; https://doi.org/10.1016/B978-0-12-809270-5.00011-X

[2] E. M. López Alejandro et al, Digest Journal of Nanomaterials and Biostructures, 18 (2023) 941-950, https://doi.org/10.15251/DJNB.2023.183.941

[3] Y. Luo, W. Guo, H.H. Ngo, L.D. Nghiem, F.I. Hai, J. Zhang, S. Liang, X.C. Wang, Science of the total environment, 473 (2014) 619-641; https://doi.org/10.1016/j.scitotenv.2013.12.065

[4] G. Crini, E. Lichtfouse, Environmental Chemistry Letters, 17 (2019) 145-155; https://doi.org/10.1007/s10311-018-0785-9

[5] S.K. Sharma, R. Sanghi, Advances in water treatment and pollution prevention, Springer Science & Business Media, 2012; https://doi.org/10.1007/978-94-007-4204-8

[6] I. Zinicovscaia, Cyanobacteria for bioremediation of wastewaters, (2016) 17-25; https://doi.org/10.1007/978-3-319-26751-7_3

[7] D.B. Miklos, C. Remy, M. Jekel, K.G. Linden, J.E. Drewes, U. Hübner, Water research, 139 (2018) 118-131; https://doi.org/10.1016/j.watres.2018.03.042

[8] A. Haruna, F.-K. Chong, Y.-C. Ho, Z.M.A. Merican, PEnvironmental Science and Pollution Research, 29 (2022) 70706-70745; https://doi.org/10.1007/s11356-022-22749-8

[9] R. Slama, J. El Ghoul, K. Omri, A. Houas, L. El Mir, F. Launay, Journal of Materials Science: Materials in Electronics, 27 (2016) 7939-7946; https://doi.org/10.1007/s10854-016-4786-9

[10] S. Santangelo, S. Patanè, P. Frontera, F. Pantò, C. Triolo, S. Stelitano, P. Antonucci, Materials Research Bulletin, 92 (2017) 9-18; https://doi.org/10.1016/j.materresbull.2017.03.062

[11] L. El Mir, Journal of Luminescence, 186 (2017) 98-102; https://doi.org/10.1016/j.jlumin.2017.02.029

[12] A. Bembibre, M. Benamara, M. Hjiri, E. Gómez, H.R. Alamri, R. Dhahri, A. Serra, Chemical Engineering Journal, 427 (2022) 132006; https://doi.org/10.1016/j.cej.2021.132006

[13] A.-I. Istrate, F. Nastase, I. Mihalache, F. Comanescu, R. Gavrila, O. Tutunaru, C. Romanitan, V. Tucureanu, M. Nedelcu, R. Müller, Journal of Sol-Gel Science and Technology, 92 (2019) 585-597; https://doi.org/10.1007/s10971-019-05144-7

[14] M.A. Qamar, W. Al-Gethami, A.-N.M. Alaghaz, M. Shariq, A. Mohammed, A.A. Areshi, Z. Khan, W. Qayyum, Materials Today Communications, (2024) 108385; https://doi.org/10.1016/j.mtcomm.2024.108385

[15] P. Mandal, J. Debbarma, M. Saha, CAppl. NanoBioScience, 12 (2023) 6; https://doi.org/10.33263/LIANBS121.006

[16] R.H. Waghchaure, V.A. Adole, B.S. Jagdale, PInorganic Chemistry Communications, 143 (2022) 109764; https://doi.org/10.1016/j.inoche.2022.109764

[17] K. Mamatha, M. Shashank, G. Nagaraju, H.S. Kumar, Journal of the Indian Chemical Society, 99 (2022) 100744; https://doi.org/10.1016/j.jics.2022.100744

[18] A.G. Oliveira, J. de Lara Andrade, M.C. Montanha, S.M. Lima, L.H. da Cunha Andrade, A.A.W. Hechenleitner, E.A.G. Pineda, D.M.F. de Oliveira, DJournal of environmental management, 240 (2019) 485-493; https://doi.org/10.1016/j.jenvman.2019.03.124

[19] A. Elhalil, R. Elmoubarki, M. Farnane, A. Machrouhi, F. Mahjoubi, M. Sadiq, S. Qourzal, N. Barka, Materials Today Communications, 16 (2018) 194-203; https://doi.org/10.1016/j.mtcomm.2018.06.005

[20] K. Ganesha, H. Chandrappa, S. Kumaraswamy, V. Annadurai, H. Somashekarappa, R. Somashekar, Non-Metallic Material Science, 5 (2023) 49-63; https://doi.org/10.30564/nmms.v5i1.5677

[21] S. Tayyaba, M.W. Ashraf, M.I. Tariq, M. Akhlaq, V.E. Balas, N. Wang, M.M. Balas, Energies, 13 (2020) 4863; https://doi.org/10.3390/en13184863

[22] M. Ashokkumar, S. Muthukumaran, Optical Materials, 37 (2014) 671-678; https://doi.org/10.1016/j.optmat.2014.08.012

[23] A. Kadam, T.G. Kim, D.S. Shin, K. Garadkar, J. Park, Journal of Alloys and Compounds, 710 (2017) 102-113; https://doi.org/10.1016/j.jallcom.2017.03.150

[24] M.M. van Rijt, S.W. Nooteboom, A. van der Weijden, W.L. Noorduin, G. de With, Materials & Design, 207 (2021) 109846; https://doi.org/10.1016/j.matdes.2021.109846

[25] L. Tairi, Y. Messai, R. Bourzami, A. Chetoui, M. Sebais, T. Tahraoui, T. Bouarroudj, H. Bezzi, D. Mekki, Physica B: Condensed Matter, 631 (2022) 413713; https://doi.org/10.1016/j.physb.2022.413713

[26] S. Selvaraj, M.K. Mohan, M. Navaneethan, S. Ponnusamy, C. Muthamizhchelvan, Materials Science in Semiconductor Processing, 103 (2019) 104622; https://doi.org/10.1016/j.mssp.2019.104622

[27] P. Visali, R. Bhuvaneswari, Optik, 202 (2020) 163706; https://doi.org/10.1016/j.ijleo.2019.163706

[28] A. Masood, T. Iqbal, M. Ashraf, A. Nazir, F. Ali, Q.A. Ranjha, M. Hussain, F. Al-Harbi, A.M. Galal, Journal of Inorganic and Organometallic Polymers and Materials, (2023) 1-14; https://doi.org/10.1007/s10904-023-02618-8

[30] A. Mirzaei, L. Yerushalmi, Z. Chen, F. Haghighat, Journal of hazardous materials, 359 (2018) 516-526; https://doi.org/10.1016/j.jhazmat.2018.07.077

[31] M. Danish, H. Ayub, Z.A. Sandhu, A. Shoaib, S. Akram, J. Najeeb, S. Naeem, Applied Nanoscience, 11 (2021) 2503-2515; https://doi.org/10.1007/s13204-021-02027-8

[32] A.T. Le, S.-Y. Pung, Pigment & Resin Technology, 50 (2020) 10-18; https://doi.org/10.1108/PRT-01-2020-0001

[33] A. Mehmood, K. Bibi, F. Ali, A. Nazir, Z.A. Sandhu, M.A. Raza, A.H. Bhalli, A. Ashraf, M. Aslam, A.G. Al-Sehemi, Journal of Molecular Liquids, (2023) 123768; https://doi.org/10.1016/j.molliq.2023.123768

[34] S.T. Tan, B. Chen, X. Sun, W. Fan, H.S. Kwok, X. Zhang, S. Chua, Journal of Applied Physics, 98 (2005); https://doi.org/10.1063/1.1940137

[35] A.K. Zak, W.A. Majid, M.E. Abrishami, R. Yousefi, Solid State Sciences, 13 (2011) 251-256; https://doi.org/10.1016/j.solidstatesciences.2010.11.024

[36] R. Abdel-Aziz, M. Ahmed, M. Abdel-Messih, Journal of Photochemistry and Photobiology A: Chemistry, 389 (2020) 112245; https://doi.org/10.1016/j.jphotochem.2019.112245

[37] A. El-Bindary, S. El-Marsafy, A. El-Maddah, Journal of Molecular Structure, 1191 (2019) 76-84; https://doi.org/10.1016/j.molstruc.2019.04.064

[38] R. Mohammed, M.E.M. Ali, E. Gomaa, M. Mohsen, Journal of Environmental Chemical Engineering, 8 (2020) 104295; https://doi.org/10.1016/j.jece.2020.104295

[39] V. Shanmugam, K.S. Jeyaperumal, Applied Surface Science, 449 (2018) 617-630; https://doi.org/10.1016/j.apsusc.2017.11.167

[40] A. Khataee, S. Saadi, B. Vahid, Ultrasonics Sonochemistry, 34 (2017) 98-106; https://doi.org/10.1016/j.ultsonch.2016.05.026

[41] P. Sreya, A.M. Mathew, B. Gowdhami, K. Vignesh, C.M. Swathi, K. Venkatesan, B. Kadalmani, D.K. Pattanayak, Surfaces and Interfaces, 42 (2023) 103425; https://doi.org/10.1016/j.surfin.2023.103425

[42] T.C. Paul, J. Podder, Applied Physics A, 125 (2019) 818; https://doi.org/10.1007/s00339-019-3112-9

[43] M.M. Ibrahim, S. Asal, Journal of Molecular Structure, 1149 (2017) 404-413; https://doi.org/10.1016/j.molstruc.2017.08.007

[44] A. Srivastava, N. Kumar, K.P. Misra, S. Khare, Materials science in semiconductor processing, 26 (2014) 259-266; https://doi.org/10.1016/j.mssp.2014.05.001

[45] A. Bishnoi, S. Kumar, N. Joshi, Microscopy methods in nanomaterials characterization, Elsevier, 2017, pp. 313-337; https://doi.org/10.1016/B978-0-323-46141-2.00009-2

[46] S. Mustapha, M. Ndamitso, A. Abdulkareem, J. Tijani, D. Shuaib, A. Mohammed, A. Sumaila, Advances in Natural Sciences: Nanoscience and Nanotechnology, 10 (2019) 045013; https://doi.org/10.1088/2043-6254/ab52f7

[47] A. Monshi, M.R. Foroughi, M.R. Monshi, World journal of nano science and engineering, 2 (2012) 154-160; https://doi.org/10.4236/wjnse.2012.23020

[48] K. Jayasankar, A. Pandey, B. Mishra, S. Das, Materials Chemistry and Physics, 171 (2016) 195-200; https://doi.org/10.1016/j.matchemphys.2016.01.005

[49] A.D. Prasetya, M. Rifai, H. Miyamoto, Journal of Physics: Conference Series, IOP Publishing, 2020, pp. 012113; https://doi.org/10.1088/1742-6596/1436/1/012113

[50] D. Nath, F. Singh, R. Das, Materials Chemistry and Physics, 239 (2020) 122021; https://doi.org/10.1016/j.matchemphys.2019.122021

[51] B. Warren, B. Averbach, Journal of applied physics, 23 (1952) 497-497; https://doi.org/10.1063/1.1702234

[52] V. Mote, Y. Purushotham, B. Dole, Journal of theoretical and applied physics, 6 (2012) 1-8; https://doi.org/10.1186/2251-7235-6-6

[53] M. Rabiei, A. Palevicius, A. Monshi, S. Nasiri, A. Vilkauskas, G. Janusas, Nanomaterials, 10 (2020) 1627; https://doi.org/10.3390/nano10091627

[54] M.B. Mobarak, M.S. Hossain, F. Chowdhury, S. Ahmed, Arabian Journal of Chemistry, 15 (2022) 104117; https://doi.org/10.1016/j.arabjc.2022.104117

[55] D. Balzar, H. Ledbetter, Journal of Applied Crystallography, 26 (1993) 97-103; https://doi.org/10.1107/S0021889892008987

[56] H. Kafashan, Materials Research Express, 5 (2018) 046417; https://doi.org/10.1088/2053-1591/aabdb8

[57] C. Muiva, T. Sathiaraj, K. Maabong, Ceramics International, 37 (2011) 555-560; https://doi.org/10.1016/j.ceramint.2010.09.042

[58] M. Kahouli, A. Barhoumi, A. Bouzid, A. Al-Hajry, S. Guermazi, Superlattices and Microstructures, 85 (2015) 7-23; https://doi.org/10.1016/j.spmi.2015.05.007

[59] S. Jaballah, M. Benamara, H. Dahman, D. Lahem, M. Debliquy, L. El Mir, Journal of Materials Science: Materials in Electronics, 31 (2020) 8230-8239; https://doi.org/10.1007/s10854-020-03358-y

[60] M. Ahmad, E. Ahmed, Z. Hong, Z. Iqbal, N. Khalid, T. Abbas, I. Ahmad, A. Elhissi, W. Ahmed, Ceramics International, 39 (2013) 8693-8700; https://doi.org/10.1016/j.ceramint.2013.04.051

[61] R.E. Adam, G. Pozina, M. Willander, O. Nur, Photonics and Nanostructures-Fundamentals and Applications, 32 (2018) 11-18; https://doi.org/10.1016/j.photonics.2018.08.005

[62] M. Hussain, A. Mehmood, F. Ali, Z.A. Sandhu, M.A. Raza, S. Sajid, M. Sohaib, M.T. Khan, A.H. Bhalli, A. Hussain, ACS Omega, (2024); https://doi.org/10.1021/acsomega.3c07251

[63] M.S. Hossain, M. Mahmud, M.B. Mobarak, S. Ahmed, Chemical Papers, (2022) 1-13.

[64] M. Danish, A. Mehmood, Z.A. Sandhu, M. Asam Raza, S. Sajid, F. Ali, ChemistrySelect, 9 (2024) e202303401; https://doi.org/10.1002/slct.202303401

[65] R. Bardestani, G.S. Patience, S. Kaliaguine, The Canadian Journal of Chemical Engineering, 97 (2019) 2781-2791; https://doi.org/10.1002/cjce.23632

[66] J.T. Held, K.I. Hunter, N. Dahod, B. Greenberg, D. Reifsnyder Hickey, W.A. Tisdale, U. Kortshagen, K.A. Mkhoyan, ACS Applied Nano Materials, 1 (2018) 989-996; https://doi.org/10.1021/acsanm.7b00398

[67] N. Kamarulzaman, M.F. Kasim, R. Rusdi, Nanoscale research letters, 10 (2015) 1-12; https://doi.org/10.1186/s11671-015-1034-9

[68] D. Sharma, R. Jha, Journal of Alloys and Compounds, 698 (2017) 532-538; https://doi.org/10.1016/j.jallcom.2016.12.227

[69] F. Ali, A. Nazir, Z.A. Sandhu, A. Mehmood, M.A. Raza, M. Hamayun, A.G. Al-Sehemi, RSC Advances, 14 (2024) 4406-4415; https://doi.org/10.1039/D3RA08311J

[70] B. Chen, H.T. Ng, C. Chen, Journal of Experimental Nanoscience, 2 (2007) 57-62; https://doi.org/10.1080/17458080601013512

[71] R. Nandini, B. Vishalakshi, Journal of Chemistry, 9 (2012) 1-14; https://doi.org/10.1155/2012/343928

[72] T. Cwalinski, W. Polom, L. Marano, G. Roviello, A. D'Angelo, N. Cwalina, M. Matuszewski, F. Roviello, J. Jaskiewicz, K. Polom, Journal of Clinical Medicine, 9 (2020) 3538; https://doi.org/10.3390/jcm9113538

[73] S.M. Mariappan, M. Shkir, T. Alshahrani, V. Elangovan, H. Algarni, S. AlFaify, Journal of Alloys and Compounds, 859 (2021) 157762; https://doi.org/10.1016/j.jallcom.2020.157762

[74] G. Yashni, A. Al-Gheethi, R. Mohamed, M. Al-Sahari, Water Practice & Technology, 16 (2021) 364-376; https://doi.org/10.2166/wpt.2020.118

[75] Y.-H. Chiu, T.-F.M. Chang, C.-Y. Chen, M. Sone, Y.-J. Hsu, Catalysts, 9 (2019) 430; https://doi.org/10.3390/catal9050430

[76] A.A. Abdel-Khalek, S. Mahmoud, A. Zaki, Environmental Nanotechnology, Monitoring & Management, 9 (2018) 164-173; https://doi.org/10.1016/j.enmm.2018.03.002

[77] F. Sadegh, W. Wongniramaikul, R. Apiratikul, A. Choodum, Environmental Technology & Innovation, 33 (2024) 103545; https://doi.org/10.1016/j.eti.2024.103545

[78] D. Toloman, A. Popa, M. Stan, M. Stefan, G. Vlad, S. Ulinici, G. Baisan, T.D. Silipas, S. Macavei, C. Leostean, Journal of Alloys and Compounds, 866 (2021) 159010; https://doi.org/10.1016/j.jallcom.2021.159010

[79] H. Agarwal, S. Menon, S.V. Kumar, S. Rajeshkumar, Chemico-biological interactions, 286 (2018) 60-70; https://doi.org/10.1016/j.cbi.2018.03.008

[80] L. Wang, H. Zhai, G. Jin, X. Li, C. Dong, H. Zhang, B. Yang, H. Xie, H. Sun, Physical Chemistry Chemical Physics, 19 (2017) 16576-16585; https://doi.org/10.1039/C7CP01687E

[81] N. Deraz, M. Selim, M. Ramadan, Materials Chemistry and Physics, 113 (2009) 269-275; https://doi.org/10.1016/j.matchemphys.2008.07.021

[82] X. Chen, Z. Wu, D. Liu, Z. Gao, Nanoscale research letters, 12 (2017) 1-10; https://doi.org/10.1186/s11671-017-1904-4

[83] G. Zhang, D. Chen, N. Li, Q. Xu, H. Li, J. He, J. Lu, Applied Catalysis B: Environmental, 250 (2019) 313-324; https://doi.org/10.1016/j.apcatb.2019.03.055

[84] C. Wu, Y.C. Zhang, Q. Huang, Materials Letters, 119 (2014) 104-106; https://doi.org/10.1016/j.matlet.2013.12.111

[85] L. Muñoz-Fernandez, A. Sierra-Fernández, O. Milošević, M.E. Rabanal, Advanced Powder Technology, 27 (2016) 983-993; https://doi.org/10.1016/j.apt.2016.03.021

[86] V. Chandraboss, L. Natanapatham, B. Karthikeyan, J. Kamalakkannan, S. Prabha, S. Senthilvelan, Materials Research Bulletin, 48 (2013) 3707-3712; https://doi.org/10.1016/j.materresbull.2013.05.121

[87] R.E. Adam, H. Alnoor, G. Pozina, X. Liu, M. Willander, O. Nur, Solid State Sciences, 99 (2020) 106053; https://doi.org/10.1016/j.solidstatesciences.2019.106053

[88] G. Nagaraju, G. Shivaraju, G. Banuprakash, D. Rangappa, Materials Today: Proceedings, 4 (2017) 11700-11705; https://doi.org/10.1016/j.matpr.2017.09.085